

JPL Document D-66493

TECHNOLOGY DEVELOPMENT FOR EXOPLANET MISSIONS

Technology Milestone Whitepaper

A Photon-Counting Detector for Exoplanet Missions

Dr. Donald Figer, PI

23 July 2010

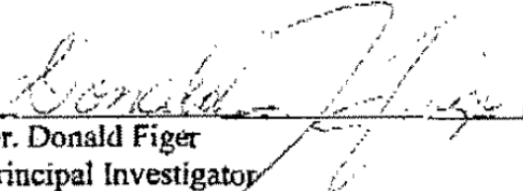
National Aeronautics and Space Administration

Jet Propulsion Laboratory
California Institute of Technology
Pasadena, California

Copyright 2011. All rights reserved.

Approvals

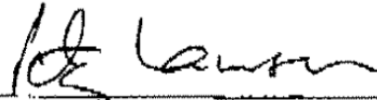
Released by



Dr. Donald Figer
Principal Investigator

8/4/10

Approved by



Peter R. Lawson
Exoplanet Exploration Program, Chief Technologist, JPL

8/9/10



Michael Devirian
Exoplanet Exploration Program Manager, JPL

8-9-10



Douglas Hudgins
Exoplanet Exploration Program Scientist, NASA HQ

8/16/2010



Lia LaPiana
Exoplanet Exploration Program Executive, NASA HQ

8-10-10

Table of Contents

Approvals.....	1
1. Objective.....	1
2. Introduction.....	1
2.1 Geiger-Mode Avalanche Photodiode	2
2.2 Previous Work.....	2
2.3 Photon-Counting Detector Design	3
2.4 Device Fabrication and Hybridization	5
2.5 Radiation.....	6
2.5.1 Radiation Effects.....	7
2.5.2 Radiation Environment	8
2.5.3 Radiation Test Program	9
2.6 Relationship to Other Activities.....	10
2.6.1 A Zero-Noise Detector for the Thirty Meter Telescope	10
2.6.2 A LIDAR Imaging Detector for NASA Planetary Missions.....	10
2.7 Comparison to CCDs with Charge Gain Registers	10
3. Milestone Procedure	12
3.1 Definitions	12
3.1.1 Read Noise.....	12
3.1.2 Dark Count Rate.....	12
3.1.3 Intrapixel response	12
3.1.4 Quantum Efficiency	12
3.1.5 Afterpulsing	12
3.1.6 Persistent Charge	12
3.1.7 Dynamic Range.....	12
3.1.8 Radiation Exposure in a Relevant Environment.....	13
3.1.9 Crosstalk.....	13
3.1.10 Estimating Rates.....	13
3.2 Measurements.....	14
3.2.1 Read Noise.....	14
3.2.2 Dark Count Rate.....	14
3.2.3 Afterpulsing	15
3.2.4 Persistent Charge	15
3.2.5 Quantum Efficiency	15
3.2.6 Crosstalk.....	15
3.2.7 Intrapixel Response	15
3.3 Milestone Validation Procedure	16
4. Success Criteria	16

5. Certification Process	17
5.1 Milestone Certification Data Package	17
5.2 The Path to Space Qualification.....	17
6. References	19
7. Team Members and Affiliations	21
8. Glossary	22

TDEM Milestone White Paper: A Photon-Counting Detector for Exoplanet Missions

1. Objective

In support of NASA's Exoplanet Exploration Program and the ROSES Technology Development for Exoplanet Missions (TDEM), this white paper describes the purpose of the TDEM Milestone for *A Photon-Counting Detector for Exoplanet Missions*, specifies the methodology for computing the milestone metric, and establishes the success criteria against which the milestone will be evaluated.

2. Introduction

This Technology Milestone serves to gauge the developmental progress of technology for a space-based coronagraph mission that would detect and characterize exoplanets, and the mission's readiness to proceed from pre-Phase A to Phase A. Completion of this milestone shall be documented in a report by the Principal Investigator and reviewed by NASA HQ. This milestone addresses measurement of the characteristics of a new photon counting array detector. The detector is a 256×256 Geiger-Mode Avalanche Photodiode (GM-APD) focal plane array that provides zero read noise, ultra-high dynamic range, and highly linear response over the relevant flux range of interest. It will deliver significant enhanced performance over existing technologies for a planet finding spectrograph, as a wavefront sensor, and for an imager.

The approach for accomplishing the milestone is to fabricate, irradiate, and test photon-counting detectors in performance metrics relevant to NASA exoplanet missions. This work will advance the technology from TRL 3 toward TRL 5, following the criteria established in NASA NPR-7120.8 App. J.¹ In particular, it will demonstrate the performance of GM-APDs in the presence of a radiation environment that is representative of a typical exoplanet mission.² The TPF-C Flight Baseline Mission Design³ defines exoplanet mission system characteristics for the purposes of this white paper. The requirement for this milestone reads as follows:

Milestone: Measure Performance of a Photon-Counting 256×256 Focal Plane Array after Radiation Exposure

Measure the following characteristics of a single-photon counting 256×256 focal plane array detector: dark current, intrapixel response, total quantum efficiency, afterpulsing, persistent charge, and crosstalk. The measurements will be made before and after 50 krad (Si) ~60 MeV proton irradiation. Important performance parameters include read noise, dark counts, and total quantum efficiency.

The detector design uses an in-pixel charge amplifying circuit that converts each absorbed photon into a relatively large voltage signal that can easily be detected by a CMOS readout circuit. The amplification is provided by a GM-APD that accelerates photogenerated charge in a region of high electric field. Each photodiode is individually bump-bonded to a silicon readout circuit. The circuitry in each pixel registers the arrival of a photon and resets the photodiode so

¹ http://nodis3.gsfc.nasa.gov/displayDir.cfm?Internal_ID=N_PR_7120_0008_&page_name=AppendixJ

² We regard radiation effects as the most critical area of concern for this technology for advancement to TRL 5, although the technology must ultimately also pass testing in the presence of other environmental conditions, e.g. heat and vibration.

³ <http://planetquest.jpl.nasa.gov/TPF-C/TPFC-MissionAstro2010RFI-Final-2009-04-01.pdf>

that it is ready to absorb another photon in ~ 100 ns.⁴ A counter in each pixel accumulates photon absorption events. The readout circuit multiplexes the digital output of the counters for each pixel through serial output registers and digital buffers.

2.1 Geiger-Mode Avalanche Photodiode

An avalanche photodiode operated in Geiger-mode produces a *digital pulse directly from the photodiode* in response to the absorption of a single photon, i.e. digitization is done in-pixel (see Figure 1). The operation of a GM-APD is conceptually simple. The APD is charged to a reverse bias voltage that *exceeds* the breakdown voltage by a few volts, and then is left in an open-circuit configuration. The absorption of a photon creates an electron-hole pair that is accelerated and multiplied in a chain of impact ionizations that creates secondary electrons and holes, just as in a traditional linear-mode APD operated below breakdown. However, the electric fields in a device biased above breakdown are strong enough that the multiplication process outpaces the extraction of carriers, resulting initially in exponential growth of current. This current growth saturates after a few tens of picoseconds because of space charge effects and device resistance. Therefore, the APD switches from an “off” state to a state in which it is conducting current. It then discharges its own capacitance until its bias falls to below breakdown, at which point the avalanche is no longer self-sustaining and the APD turns off. With appropriate biasing of the APD, this discharge voltage pulse is level shifted to fall within a CMOS-logic-compatible range. Once the APD has had adequate time to turn off and release any trapped carriers, it can be reset for the next detection.

Detectors based on this principle digitize photon arrival times or rates within the pixel circuit; therefore, they have quantum-limited sensitivity and zero readout noise. While the GM-APDs need several tens of volts to be biased in the Geiger mode, only digital-like voltage transitions are required to operate the detector, thereby avoiding the power dissipation and mass associated with analog digitizing circuits. They are resilient to radiation for several reasons, but primarily because the signal charge is not clocked across charge traps in neighboring pixels, e.g. as in a conventional CCD.

2.2 Previous Work

The design used for this project is evolved from a series of devices designed by Lincoln Laboratory (See Figure 2; Cova et al. 1996, Albota et al. 2002, Aull et al. 2005, 2006). The sensitivity and noise-free readout of these devices provided significant benefits in system performance. In these applications, accuracy in timing of individual photon events is the most important performance metric. Previous LIDAR demonstrations validated the utility of photon-counting detector array technology, in particular for tactical military applications (Marino et al. 2003).

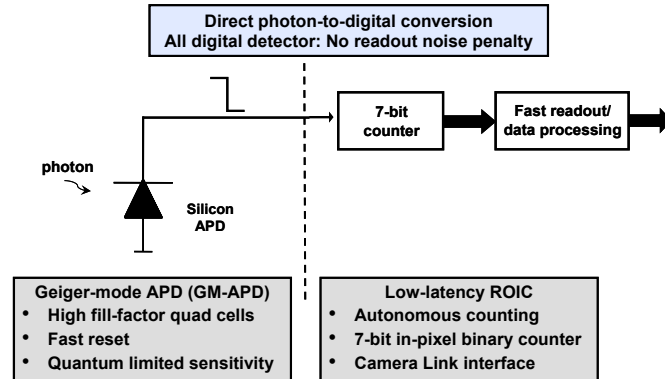


Figure 1. Schematic representation of an APD pixel. The photodiode circuit generates a digital pulse for each incoming photon. Events are accumulated by an in-pixel counter before being read out.

⁴ This is a relatively long time when considering the very low flux levels expected for an exoplanet mission. For instance, in spectroscopic mode, the flux is ~ 0.2 photons/s.

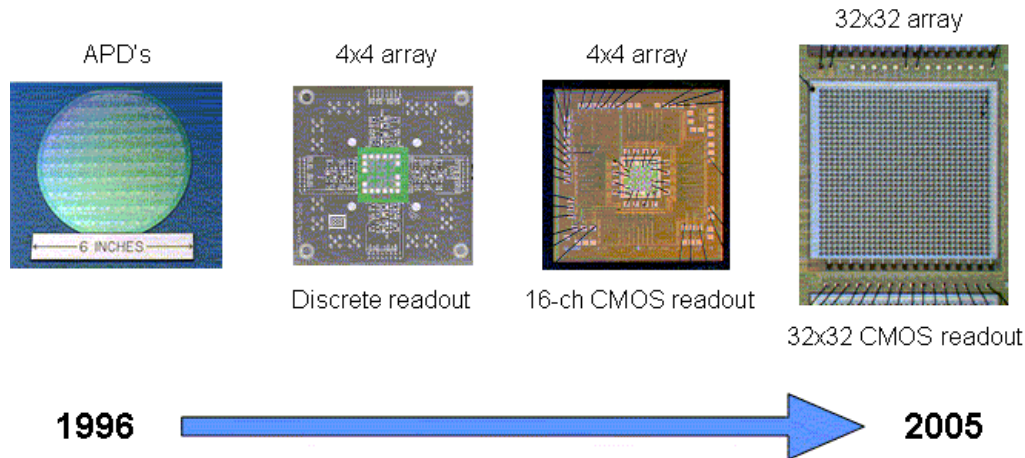


Figure 2. Evolution of Lincoln Laboratory LIDAR APD arrays.

Development of this technology at Lincoln Laboratory started in the mid 1990's, with initial interest focused on tactical military laser radar imaging. In 1997, the principle of “photon-to-digital” conversion was demonstrated by wire bonding the 4x4 APD array shown in Figure 2 to a CMOS chip with 16 digital timing circuits. The simplicity of direct connection between detector and CMOS logic was an enabler for building 3D imaging systems. The arrays were scaled up to 32x32 format and techniques were developed to hybridize to CMOS readouts. By 2005, hybridized arrays with timing resolutions in the 250 ps range had been fabricated, packaged, and incorporated into airborne laser radar systems that demonstrated foliage penetration and rapid terrain mapping. The APDs developed for these systems are inherently low fill factor devices (5-7%), and light concentration was achieved either by using microlenses or by transmitting an array of light spots onto the scene.

This success aroused interest in other applications in which the photons are counted rather than time stamped. Arrays of specialized Geiger-mode quad-cell detectors were developed as Shack-Hartmann wavefront sensors for high-frame-rate adaptive optics applications. By 2008, it was demonstrated that the quad cell had high fill factor. A 16x16 quad-cell array was reported with 40% detection efficiency and sub-kHz dark count rate at -20°C .

Current efforts are focused on development of larger format (256x256) high fill factor APD arrays for passive imaging, as is needed for the current project. A novel CMOS readout architecture was developed that simultaneously provides a small pixel (25 μm), high dynamic range, and low readout bandwidth. Learning from the experience with the quad-cells, Lincoln Laboratory is developing new APD structures that will combine high detection efficiency (>70%) with low dark count rate (sub-kHz with modest TE cooling).

Two new improvements for the current project are the use of a larger photon absorbing region and a bonded architecture that allows for backside illumination. These features combine to deliver high fill factor compared to previous LIDAR pixel designs which have relatively low fill factor. This is particularly important for imaging very faint point sources, where it is important to collect every photon and preserve uniform sensitivity across the pixel area.

2.3 Photon-Counting Detector Design

The proposed detector has two components, the GM-APD array and the CMOS readout. The GM-APDs consist of an absorber region, which converts incoming photons to electron-hole pairs, and a multiplier region that accelerates the photogenerated charge, thereby causing a

charge avalanche. The probability that an avalanche will occur is primarily dependent on the applied bias voltage that holds the diode above the breakdown voltage.

Figure 3 shows a cross-section of two versions, one using a low-fill-factor design and the other using a high-fill-factor design. Both designs are intended to be used in a backside illuminated configuration, as opposed to earlier devices that had all been used with frontside illumination. On the right of the figure, the shallow portion of the stepped p+ implant separates the absorber and multiplier portions of each detector. The step lowers the electric field at the edges of the diode, preventing edge breakdown and forming a guard ring to collect surface-generated dark current without multiplying it. The deep portion of the implant, which is partially undepleted, prevents the guard ring from collecting photoelectrons generated in the absorber; as indicated in the figure, these photoelectrons reach a nearby multiplier region by a combination of diffusion and drift.

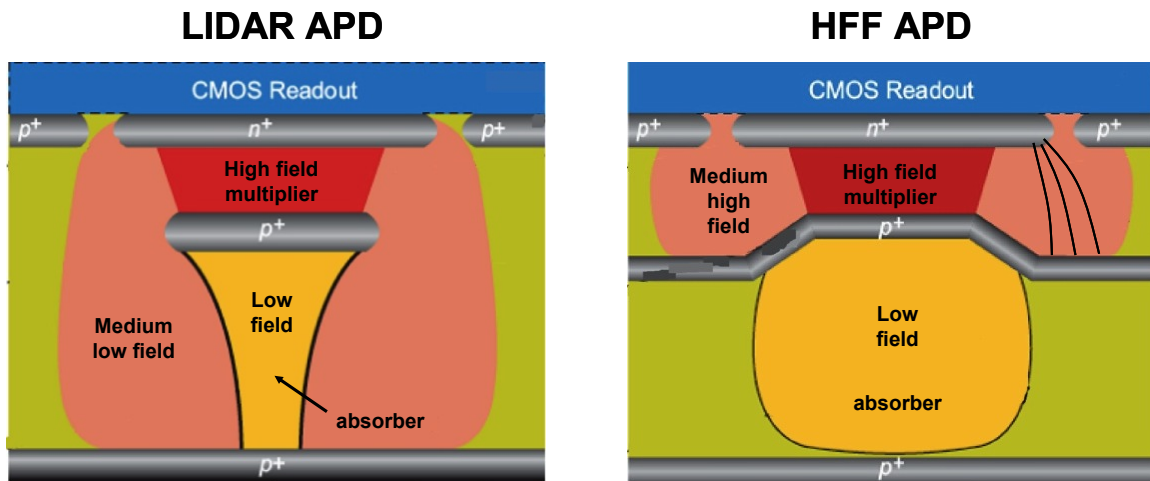


Figure 3. Cross-sections of two APD designs, one using a low-fill-factor design suitable for LIDAR (left) and the other using a high-fill-factor design suitable for imaging applications (right). Photons are absorbed in the “absorber” regions. Charge is multiplied in the “multiplier” regions.

A 256×256 CMOS ROIC has been designed with 25 μm pixels, based on an innovative approach to managing the tradeoff between pixel real estate and readout bandwidth. Each pixel has a flip-flop that is set whenever a photon detection has occurred. In addition, there is a modest-sized (7-bit) counter that counts detection events. When the 7-bit counter overflows, it sets an overflow flip-flop and continues counting from zero. The chip has two independent readout systems, one for reading out the detection flip-flops and another for reading out the counter overflow flip-flops. Each system addresses successive rows or columns of pixels, reading out and clearing the flip-flops, while the pixels continue to stare and register events. For low fluxes, individual detection events can be recorded. At higher fluxes, the overflow bits can be recorded; each represents the detection of 127 photons. There is also a mechanism to readout the entire contents of the 7-bit counters.

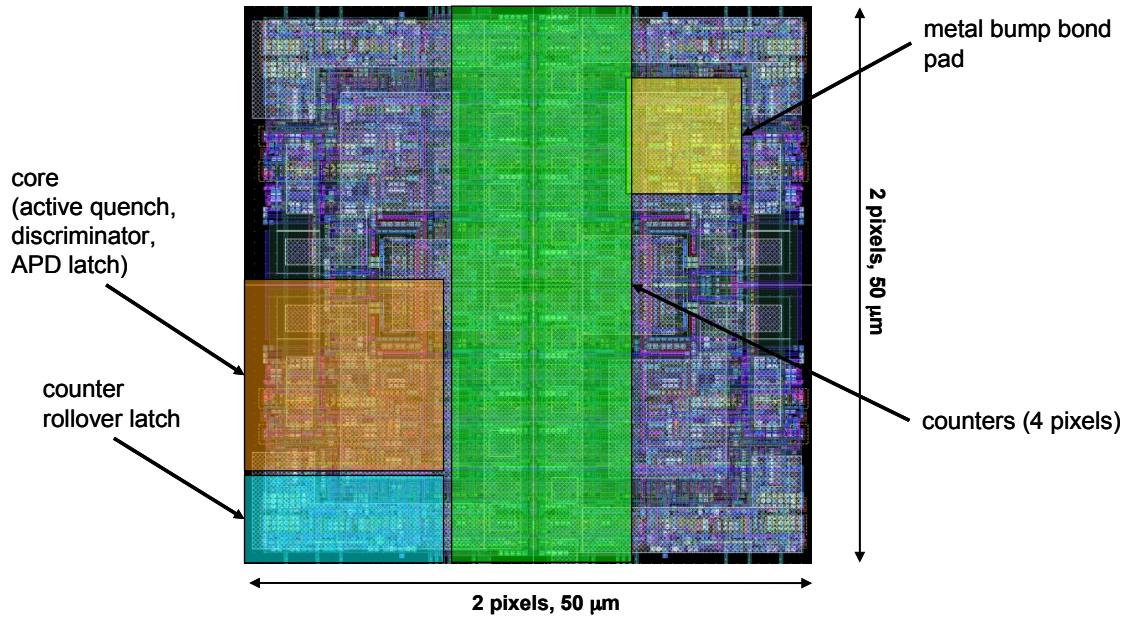


Figure 4. Close-up of the 256×256 ROIC layout, covering a 2×2 pixel area. The counter blocks for all four pixels form a contiguous region. Each pixel has its own isolated core, counter, and bump bond pads, although only one of each is highlighted in this representation.

2.4 Device Fabrication and Hybridization

The ROIC has been fabricated through MOSIS using an IBM 180 nm process to fit the circuitry into a small pixel format. The GM-APD array will be fabricated in Lincoln Laboratory’s Microelectronics Laboratory. Starting with a lightly p-doped epitaxial layer on a p+ silicon substrate, the high-fill-factor device structure (Figure 3) will be fabricated through a series of masked ion implantation steps. The stepped p-implant profile will be achieved by implanting boron through an oxide mesa. Westhoff et al. (2007) give a good review of these, and other associated steps in this process.

Back-illuminated APDs that can be bump bonded to CMOS readout chips will be made by replacing the original silicon substrate with a quartz substrate for both the low and high fill factor cases. The APD wafer will first be bonded on the front side to an oxidized silicon handle wafer. Then the APD substrate will be removed by a combination of grinding and chemical etching. The exposed backside will then be passivated with a p+ contact layer, oxidized, planarized, and bonded to the quartz substrate. The handle wafer will then be removed. The remaining hybridization process is conventional. Indium bumps will be patterned on the APD contact pads, the wafer will be diced, and the die will be bumped to mating CMOS readout chips.

Table 1 highlights the most important fabrication steps in this project. Lower-fill-factor APD technology is mature enough at this stage to deliver detectors that feature them relatively early in the project, so they can be delivered in year one of the project. These devices will be key for validating performance of the light sensitive layer and the new 256×256 ROIC on which it will be bonded; note that this will be the first time validating operation of the ROIC that is now being fabricated for another project. If the low-fill-factor detectors perform as expected, then they could be used in an exoplanet spectrograph with microlenses to increase net fill factor. Next, high-fill-factor detectors will be fabricated. These are expected to have near unity fill factor. Finally, we will fabricate a process lot of APDs with a new design that is intended to lower dark counts.

It may also be useful to fabricate and package individual APDs for independent radiation testing that would not include the high density ROIC. This type of testing can be used to separate

radiation effects in the ROIC from such effects in the light-sensitive material. We will consider doing this type of radiation testing within the constraints of schedule and funding.

Table 1. Summary list of detector fabrication tasks.

<p>1. Early Delivery of 256×256 Detector with Conventional GM-APDs</p> <p>Conventional (low-fill-factor) GM-APDs will be hybridized to the 256×256 CMOS ROIC. These LIDAR-style APDs will be used so long exposures (requiring low dark current) are possible. To improve fill factor, microlenses may be attached to the detector array. Five integrated sensors and CMOS ROICs will be packaged and characterized by LL. A replica of the electronics, which are now being designed in another project, will be built for the TDEM project. The packaged sensors and electronics set will be provided to RIT for doing the laboratory experiments to validate performance for TDEM. The test results will also be used to redesign the GM-APD.</p>
<p>2. Fabrication of 256×256 Detector with High-Fill-Factor GM-APDs</p> <p>High-fill-factor GM-APDs will be integrated with the CMOS ROIC. The GM-APDs will be the most recent version. Five devices will be fabricated for laboratory and radiation beam testing relevant to TDEM.</p>
<p>3. Design Iteration for Improved High-Fill-Factor GM-APDs</p> <p>A mask set will be generated with design changes to the 256×256 GM-APD array that will improve device performance, such as dark counts. The new masks will include test structures to evaluate GM-APD performance. A process lot of GM-APDs will be fabricated through front-illuminated processing. The lot will have process modifications that have the potential to further reduce dark counts below those of existing APDs; these modifications will take advantage of laboratory and radiation test results from the low and high-fill-factor devices. The performance of the front-illuminated process lot will be measured.</p>

2.5 Radiation

Radiation testing is the most important step in advancing GM-APD detectors to TRL 5. While other types of testing will also eventually need to be done, the technologies used in this program are directly derived from previous technologies that have successfully passed vibration and thermal testing, including those that have already flown in space. In particular, we will use the same legacy packaging techniques that have been used on all the NASA missions in which Lincoln Laboratory have supplied packaged detectors (ASCA, Chandra, Suzaku, EVE, etc.). The packaged GM-APDs will have the same NASA-qualified epoxies and bond wiring techniques. This includes bond pull testing of every bond wire to specification. The satellite-based package devices mentioned have been vibration, shock, and temperature tested to the specification of the stated missions.

The effects of radiation on the CMOS ROIC and GM-APDs will be determined by modeling and experiment, following a plan similar to that described in the European Space Agency's (ESA) handbook ECSS-E-HB-10-12 and with guidance from JPL Publication 00-06.⁵ The radiation environment on orbit will be determined using models from programs such as SPENVIS and SPACERAD and the amount transported through shielding will be calculated. Initially, a simple spherical shell of variable thickness will be used to simulate the shielding and a margin of 2x will be assumed for the intensity of the radiation spectra (protons, electrons, and

⁵ "An Introduction to Space Radiation Effects on Microelectronics" (<http://parts.jpl.nasa.gov/docs/JPL00-62.pdf>), "Standards for Space Radiation Environments and Effects" (<https://escies.org/GetFile?rsrcid=307>)

cosmic rays). The effects of radiation will be determined on the basis of ionizing and nonionizing radiation. Generally, the ionizing radiation effects on such characteristics as dark-count rate scale with total ionizing dose (TID), while those of nonionizing radiation scale with nonionizing energy loss (NIEL). The NIEL, as a function of particle energy, can be generated by programs such as SRIM. The relative change in a property of interest can be determined in a given radiation environment by measuring the response to high energy protons, say, 63 MeV, and scaling that response through the TID and NIEL tables to the integrated spectrum. This approach has worked well in space-qualifying several missions for imagers for NASA (Chandra, ASCA, SUZAKU, HETE).

As an example, relating the change in dark current for a proton spectrum to the change in dark current ($\Delta I_D(\text{spectrum})$) for samples exposed to 63 MeV radiation ($\Delta I_D(63\text{MeV})$),

$$\frac{\Delta I_D(\text{spectrum})}{\Delta I_D(63\text{MeV})} = \frac{\int \text{NIEL}(E)\phi(E)dE}{\text{NIEL}(63\text{MeV})\phi(63\text{MeV})FWHM(63\text{MeV})}, \quad \text{Equation 1}$$

where $\text{NIEL}(E)$ and $\phi(E)$ are the energy-dependent NIEL and flux of the proton spectrum (transported through any shielding) on orbit, $\text{NIEL}(63\text{MeV})$ and $\phi(63\text{MeV})$ are the NIEL and flux used in the proton irradiation experiment on earth, and $FWHM(63\text{MeV})$ is the full-width half-maximum energy spread of the proton beam. The energy of 63 MeV has been used widely for testing CCDs since it is near the peak flux for several low-earth orbit spectra and it is the energy of the proton beam at the University of California, Davis accelerator.

2.5.1 Radiation Effects

High energy radiation affects focal plane detectors in a number of ways. These include increased dark current, threshold voltage drift, latch-up, and single-event upsets. Some of these effects are transient and can be completely mitigated through thermal annealing or even initiating a new exposure. Other effects contribute to cumulative degradation of performance during a mission lifetime. The short term effect of this radiation is a slight degradation in signal-to-noise ratio. The long term effects could be degradation in several categories. For a hybridized APD/CMOS focal plane, such as the one proposed here, there are effects specific to the each of the two components, the CMOS circuitry and the Geiger-mode avalanche photodiodes.

For the CMOS circuitry, ionizing radiation can produce single-event upsets that cause bit errors and, in the case of a bulk CMOS process, latch-up. Nonionizing radiation, on the other hand, produces damage that accumulates with dose. For CMOS circuits, this takes the form of charged defects in the gate and field oxides, which respectively shift transistor turn-on voltages and create parasitic leakage paths. Eventually, these total-dose effects can cause circuit malfunctions. One advantage of the Geiger-mode technology is that the CMOS pixel circuit is all digital, making it more robust than analog circuitry to total-dose effects.

Techniques for making the CMOS radiation hard are well known. They include circuit design and layout approaches, scaling to thinner gate oxides, and the use of silicon-on-insulator (SOI) CMOS technology. The photon-counting ROIC used in this effort was designed in a bulk 180 nm CMOS process under funding from another project. Radiation hardness was not a goal of the design, but we believe that there is a straightforward path to achieving it.

The principle concern in our effort is the radiation tolerance of the Geiger-mode APDs. These detectors are inherently tolerant to single-event upsets, because even a large packet of charge produced by a high-energy particle or photon tends to trigger a single detection event. Nonionizing radiation, on the other hand, produces traps in the silicon that increase dark current, and therefore dark count rates, over time.

Previous measurements at Lincoln Laboratory have shown that a 24- μm pixel CCD has an increase in dark current of about 0.7 e-/pix/s/(total rad) of 40 MeV protons at -20°C . Fortunately, the pixel area is close to that of a GM-APD array of 25 μm cells, but the change

will scale with area. Cooling will also reduce the dark current. The effect of temperature on dark count rate has been modeled as proportional to $e^{-\Delta E/kT}$, where ΔE is the activation energy, k is Boltzmann's constant, and T is the temperature. We have found that ΔE is greater than 0.6 eV, half the energy gap of Si, indicating the dark count rate is typical of a well-behaved Si diode. Assuming a drop in temperature to -100 °C and exposure to 5 krad (Si) radiation at 40 MeV, we would expect an incremental increase in dark current of 0.005 e-/pix/s.

2.5.2 Radiation Environment

The radiation testing program for this project assumes a five year mission lifetime and a spacecraft location at L2, given that the majority of proposed exoplanet missions would be located there (see Table 2). At a location of L2, we expect the cumulative dose to be ~ 5 krad (Si) for a five year mission lifetime and average solar activity. Given this level of dose, we expect ~ 5 -10 ions/s/cm² that would produce “false” events (Rauscher et al. 2004).

Table 2. List of potential future exoplanet missions.

Mission ⁶		Location
SIM Lite		Earth-trailing heliocentric
Telescope for Habitable Exoplanets and Interstellar/Intergalactic Astronomy	THEIA	L2
New World Observer	NWO	L2
Terrestrial Planet Finder	TPF-C	L2
Extrasolar Planetary Imaging Coronagraph	EPIC	Earth-trailing heliocentric
Giant planets around M, L, T dwarfs in the Infrared	GIMLI	Earth-centered distant retrograde orbit (semimajor axis: 700,000 km)
Pupil-mapping Exoplanet Coronagraphic Observer	PECO	Heliocentric drift away orbit (like Kepler and Spitzer)
Transiting Exoplanet Survey Satellite	TESS	Low Earth Orbit (600km equatorial orbit)
Fourier-Kelvin Stellar Interferometer	FKSI	L2
PLANetary Transits and Oscillations of stars	PLATO	L2
All Sky Transit Observer	ASTrO	L2
The Terrestrial and Habitable-zone Exoplanet Spectroscopy Infrared Spacecraft	THEISIS	L2

We simulated the expected radiation environment at L2. A sample plot of integrated fluence versus particle energy for solar protons at L2 is shown in Figure 5. The total dose over the mission lifetime is dependent on the relative phasing between the mission launch date and the solar cycle. It also will depend on the frequency and severity of solar storms during mission lifetime.

⁶ Taken from the “Exoplanet Forum 2008” (http://exep.jpl.nasa.gov/exep_exfPresentations.cfm)

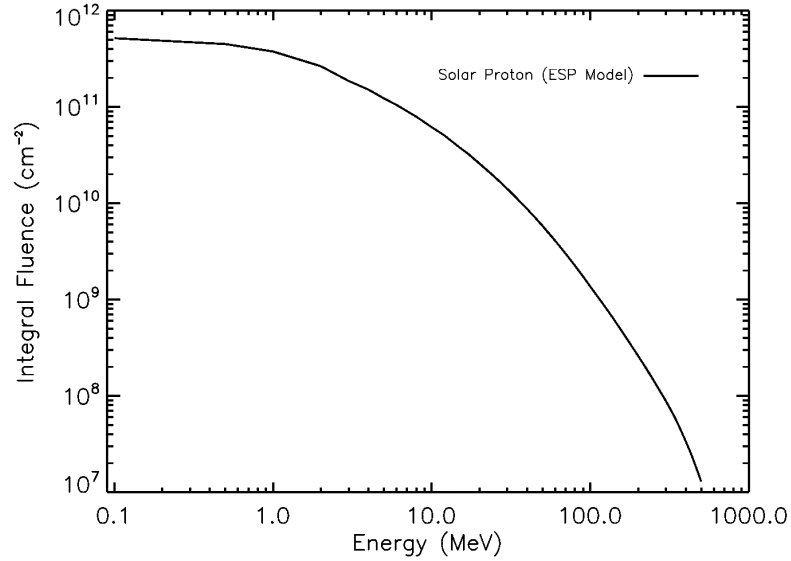


Figure 5. Integrated fluence versus particle energy for solar protons at L2, assuming a launch date of 2014 and a mission duration of five years. At L2, contributions from trapped electrons and protons are negligible, so are not included.

2.5.3 Radiation Test Program

The first step in designing a radiation testing program is to simulate the radiation field in the eventual operating environment, as described in Section 2.5.2. Second, the radiation field must be propagated through the spacecraft shielding which has the effect of attenuating particle energy and transmission. Results from a simulation of simple shielding are shown in Figure 6. Third, the transported radiation must be translated into detector effects, the most severe of which have already been described above. Fourth, and finally, a ground-based test program must be designed to simulate the expected environment and radiation effects for a focal plane in space.

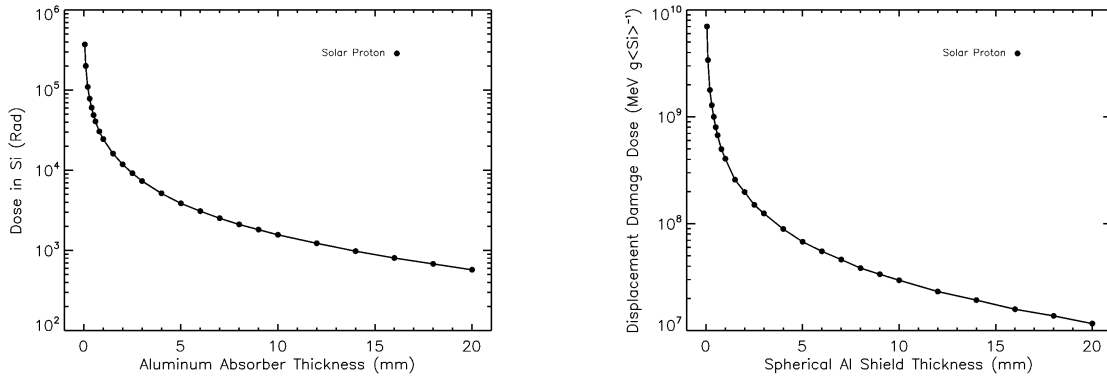


Figure 6. Cumulative total ionizing dose (left) and nonionizing dose (right) of space radiation for a five-year mission at L2 versus shield thickness, for spherically-shaped aluminum shielding. For a shield thickness of 1 cm, the total expected ionizing dose is approximately ~4 krad (Si).

This last step requires significant interpretation because the variety of energies and particles in space will normally exceed what is practically available on the ground, where it is often the case that monoenergetic high energy protons are the only radiation source used in testing. As related above, the particle spectrum will be convolved with the results obtained at a

particular energy to predict the effects on the devices. Figure 7 shows the nonionizing fluences of monoenergetic protons that produce the same damage as the spectrum of radiation shown in Figure 5. Depending on the chosen energy for ground based radiation, these plots indicate the fluences that accurately mimic the damage expected in space.

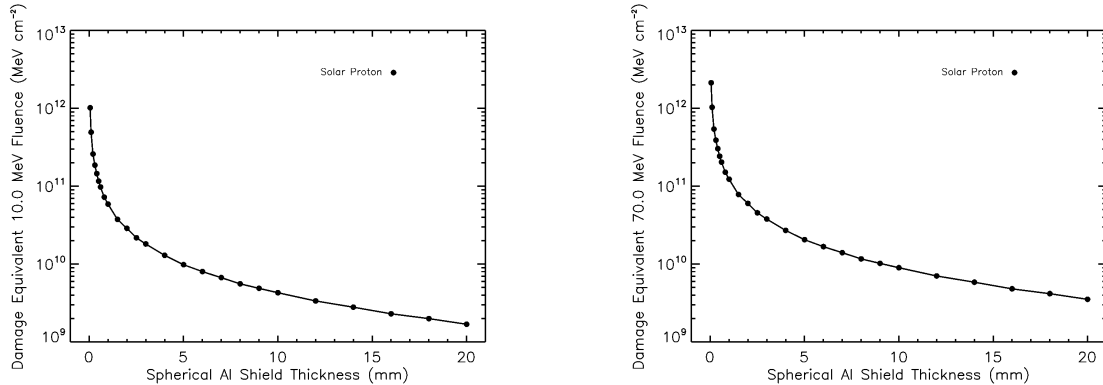


Figure 7. Fluences that predict the same nonionizing damage as would be expected for a five year mission at L2, assuming a beam of 10 MeV (left) and 70 MeV (right) protons.

2.6 Relationship to Other Activities

2.6.1 A Zero-Noise Detector for the Thirty Meter Telescope

This project is led by Rochester Imaging Detector Laboratory and is a collaborative effort with Lincoln Laboratory. The Moore Foundation has funded this project to deliver infrared (InGaAs) megapixel imaging arrays based on GM-APD arrays and event counting multiplexors for ground-based applications. They are zero-noise in the sense that a single photon is able to trigger a response well outside the noise band of the detector circuit. It is incumbent on the circuit designer to make use of this technological advance in processing the signal. Silicon devices are being designed and fabricated as pathfinders to the infrared devices. The designs in this project will serve as starting points for the designs in the TDEM project. The TDEM project will use more devices than the Moore project is producing, some of which will be irradiated in a proton beam.

2.6.2 A LIDAR Imaging Detector for NASA Planetary Missions

This project is also led by RIDL and is a collaborative effort with Lincoln Laboratory. It will produce low fill factor 32×32 pixel LIDAR imaging detectors. In these devices, the readout circuitry records photon time of arrival, instead of number of photon events. The light-sensitive arrays contain GM-APDs.

2.7 Comparison to CCDs with Charge Gain Registers

There are other array detector technologies that deliver photon-counting capability, e.g. electron-multiplying CCDs (EMCCDs), a specific example of which is the L3CCD (Low Light Level CCD) made by e2v Technologies, Ltd. This device has been used for fast imaging in ground-based applications (Daigle et al. 2009). It had also been considered (and rejected) for the space-based GAIA mission (Pool et al. 2005). By applying high gain at the output of a conventional CCD, the EMCCD enables photon counting at low fluxes. The advantage is lost when the flux contributes more than one electron of integrated charge per pixel per read time interval. In this case, photons are “lost” (see Figure 8).

An alternative is to operate the device in linear mode, in which the amplified signal is translated into the number of events that generated the signal; then the effective shot noise is increased by a factor of root two higher than even a conventional CCD because of uncertainty in the gain. Note that the TPF “test case” of an Earth-like planet around a Sun-like star usually does not consider the possibility of extended emission around the star. When such emission is present, it is important that the detector be able to deliver SNR limited by the shot noise from the collected flux. Therefore, it is important to use a detector that preserves the advantages of photon-counting at arbitrary flux levels. Having the electron multiplying stage at an output, instead of inside of each pixel, limits the length of the read time window because many pixels must be read through the same output before the device can be clocked through a new exposure.

One way to ensure that only one event is counted per read is to dramatically increase the read rate. One consequence of this approach is that clock induced charge (CIC) is increased. This effect contributes an effective dark current noise contribution to the output signal. In effect, then, the desire to limit events to single photons competes with the desire to minimize spurious charge. Even after mitigation effects (inverted clocks), CIC generates about 0.0015 e-/pixel/read in spurious charge at -20 C. If the device is read at 10 Hz frame rate for a 1 minute exposure, that implies 600 reads, or 0.9 e-/pixel, enough to generate a false event 90% of the time. While CIC can be reduced with additional cooling, it still degrades SNR.

There are other important effects in EMCCDs, e.g. charge bleeding at temperatures below -100 C (Daigle et al. 2008), gain instability, CTE loss at low temperature, and typical radiation-induced CTE with exposure to space radiation. The EMCCD is more susceptible to radiation damage than traditional CCDs (Hadwen et al. 2004; Smith et al. 2006; Pool et al. 2005). This is due to radiation-induced energy states between the valence and conduction bands near the high field regions of the gain register elements. After exposure to 5 krad (Si) in high energy protons, the sum of the induced dark current in the output and gain registers is 0.4 e-/gain element/pixel for a nominal read rate of 11 MHz at -20 C (Mark Robbins, e2v, 2009, private communication). A Monte Carlo simulation predicts an average output charge of about 500 e-/pixel from this contribution. Cooling will help reduce this effect, but it will always be present in an EMCCD.

As a point of comparison, note that the GM-APDs have a measured dark count rate of 2 events/s/pixel at 215 K for a device with 50 μm pixels and a demonstrated exponential reduction of this rate with temperature. Extrapolating to 170 K and 25 μm pixels, one expects a dark count rate of 0.0001 events/s/pixel. Of course, other sources of dark current will likely dominate at this temperature.

Other important effects produced by GM-APDs that can degrade SNR include afterpulsing and crosstalk. Both of these are being minimized in the current project using new design features that leverage a base of data from previous design and testing programs.

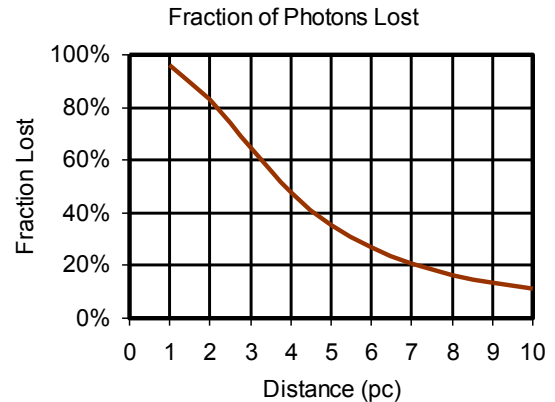


Figure 8. Fractions of photons lost for an EMCCD, assuming a 1 second frame time and flux from an Earth-like planet at a range of distances near a Sun-like star with a suppression factor of 10^{10} .

3. Milestone Procedure

3.1 Definitions

Each application demands detector performance levels in a particular set of characteristics. For instance, exoplanet spectroscopy depends on very low noise detectors. A key challenge for the system is to detect a planet that contributes a very faint flux of about 0.2 photons/s ($R=30$ mag) distributed over a photometric aperture. For a critically sampled point spread function, this corresponds to a flux of about 0.1 photons/s/pixel for the central pixel. Spreading this flux across the focal plane of a spectrograph leads to even fainter fluxes. Assuming $R \sim 100$ ($=\lambda/\Delta\lambda$), the resultant flux will be about 20 photons/hour/pixel. Potential noise sources for both spectroscopy and imaging are read noise, shot noise from the residual light from the star, shot noise from the zodiacal light, and shot noise from dark current. The following definitions are used in this document.

3.1.1 Read Noise

Read noise is the uncertainty in the estimated signal value produced by a detector exposed to no light and having negligible dark events per exposure. It is defined to be an intrinsic property of the light-sensitive structure and the readout circuit. It does not include shot noise from any source or noise in downstream electrical components, e.g. cables, amplifiers, and analog-to-digital converters.

3.1.2 Dark Count Rate

Dark count rate is the rate of events generated at the readout circuit output while the detector is in complete darkness. Note that this can differ from dark current, some fraction of which might not generate events; this is the case for dark charge that is not amplified enough to trigger the event discriminating circuitry in the readout circuit.

3.1.3 Intrapixel response

Intrapixel response describes the uniformity of response across the full area of the pixel.

3.1.4 Quantum Efficiency

Quantum efficiency is the ratio of detected events to incident photons. It is the product of several probabilities: transmission, absorption, diffusion, amplification, and triggering.

3.1.5 Afterpulsing

Afterpulsing describes the tendency of an individual APD pixel to produce a burst of events after an avalanche has been initiated and quenched in that pixel. An afterpulse can be triggered when charge produced in the original avalanche becomes trapped in material defect sites and later migrates from the trap to the high field region. It can also be produced if charge from the original avalanche is temporarily stored in the absorber region while the depletion region is debiased. Afterpulsing is a function of avalanche time, quench time, pixel geometry, field geometry, biasing, and the trap population.

3.1.6 Persistent Charge

Persistent charge is the charge that becomes trapped in the light-sensitive portion of the detector and then becomes liberated and counted as events in later exposures.

3.1.7 Dynamic Range

Dynamic range is the ratio of the maximum to minimum signal.

3.1.8 Radiation Exposure in a Relevant Environment

Radiation exposure in a relevant environment describes exposure of a device to radiation flux, fluence, energy distribution, and particle distribution that mimics the expected exposure in a mission design.

3.1.9 Crosstalk

Crosstalk generates events in one pixel as a result of activity in another pixel or output channel. It can be induced by electrical interference, charge diffusion or photon generation during charge avalanche. For the architecture used in this project, the output signals are converted to digital form in the pixel circuit, so electrical crosstalk that normally affects weak analog signals in most detectors will not be important. Charge diffusion is as much a concern in the current architecture as it is for any detector. Optical crosstalk is potentially more of a discriminator for comparing the current architecture to that of typical detectors. This is because the photoexcitation of nearby pixels depends on photoemission in the avalanche process.

3.1.10 Estimating Rates

The measured event rates will be reduced from the true rates due to detector dead time. There are two types of dead time in the system being designed. One is due to the APD quench/reset time; this is on the order of 100 ns. The other is due to the finite polling time of the system. This time sets the minimum time after which a pixel has initiated an avalanche that the pixel counter can record that event. For example, if a photon generates a charge avalanche halfway through a clock cycle, then that will generate a “high” pixel state in the next clock cycle. In this sense, the pixel is “dead” to new photons for half of the first cycle time plus one full cycle during which the event count flag is high. Figure 9 shows a representation of the relevant events.

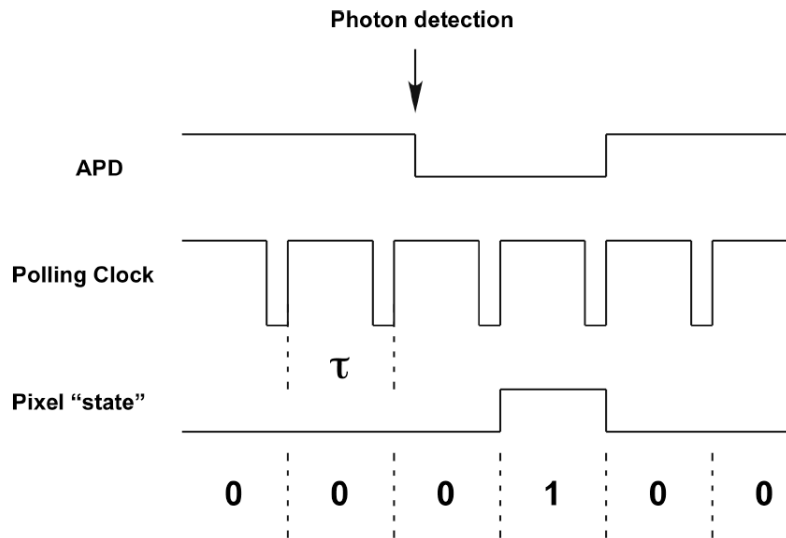


Figure 9. Clock diagram showing the timing relationship between photogenerated events and system state. Note that the same relationships hold for dark current generated events.

The counted events can be used to estimate the number of events that would have been counted in the absence of dead time. The mathematical relationship between the two is given in Equation 2.

$$\bar{c} = N \frac{1 - e^{-\rho\tau}}{2 - e^{-\rho\tau}}, \quad \text{Equation 2}$$

where \bar{c} is the counted events, N is the number of cycle times, ρ is the expected rate in the absence of dead time and τ is the cycle time. Note that in the upper limit of high flux, measured counts will be equal to one half of the number of cycles. This is because the cycle following an event will be lost to system dead time, as shown in Figure 9. The variance, $\bar{\sigma}_c^2$, is given in Equation 3.

$$\bar{\sigma}_c^2 = N \frac{(1 - e^{-\rho\tau})e^{-\rho\tau}}{(2 - e^{-\rho\tau})^3}. \quad \text{Equation 3}$$

For the purposes of this project, results will be reported in both counted events and inferred expected number of events. For best results, we will attempt to obtain data in regimes where this correction is not important, i.e. the fluxes are low. This formulation, and strategy, is valid both for photo-induced events and multiplied dark current-induced events.

3.2 Measurements

The following subsections describe the methods that will be used to measure relevant detector performance in this project. In general, a measurement is successful if it is repeated three consecutive times with median results that are consistent within 10%. For some experiments, the system needs to shield the detector from light. In these cases, the system shall be dark enough over the visible waveband (300 nm to 1100 nm) to be a negligible contributor to dark count events induced by the detector down to a level of 0.001 events/s/pixel.

3.2.1 Read Noise

1. Blank off the system so that no light falls on the detector.
2. Idle the system at operating temperature for at least 10 hours so that persistent charge has a chance to become liberated.
3. Obtain dark images with exposure times of one second.
4. Make a single FITS image per exposure. Each pixel value shall be the sum of all events during the exposure for that pixel divided by the exposure time.
5. Expose the detector to a low level light source and obtain another set of dark images.
6. Increase the light level in small increments and repeat step #4.
7. Compute variance divided by number of events for each pixel.
8. Make a histogram of the ratios computed in step #7 and report the median and cumulative distribution.

3.2.2 Dark Count Rate

1. Blank off the system so that no light falls on the detector.
2. Idle the system at operating temperature for at least 10 hours so that persistent charge has a chance to become liberated.
3. Obtain dark images with exposure times of at least one hour.
4. Make a single FITS image per exposure. Each pixel value shall be the sum of all events during the exposure for that pixel divided by the exposure time.
5. Repeat steps 4 and 5 for temperatures from 150 K to room temperature, inclusive, in steps of 20 K.
6. The dark count rate shall be reported as the median pixel value in the FITS image.
7. Make a histogram of dark count rates, with a legend that records the median, cumulative distribution, number of hot pixels, and number of dead pixels.

3.2.3 Afterpulsing

1. Program the readout electronics so that an individual pixel can be armed, quenched, reset, and read as fast as possible.
2. Run the code in step one.
3. Illuminate the detector with a fast laser pulse ($\tau_{\text{width}} < 10$ ns).
4. Record all events for ten seconds after the pulse.
5. Repeat steps one through four in order to generate a statistically significant data set.
6. Plot the time autocorrelation of the data sets.

3.2.4 Persistent Charge

1. Blank off the system so that no light falls on the detector.
2. Idle the system at operating temperature for at least 10 hours so that persistent charge has a chance to become liberated.
3. Obtain series of dark exposures.
4. Illuminate detector while taking exposure.
5. Put closed filter position in place.
6. Perform a number of resets of detector.
7. Take 2000-second persistence exposure.
8. Repeat steps three – seven for three levels of flux (TBD).
9. Plot median signal versus time for persistence exposure.

3.2.5 Quantum Efficiency

1. Illuminate the detector with a narrowband ($\Delta\lambda=10$ nm) monochromator source.
2. Obtain exposures at wavelengths from 300 nm to 1100 nm, every 10 nm.
3. Repeat the same setup, but this time with a calibrated diode at the location of the detector.
4. Plot the number of events divided by the calibrated number of incident photons as a function of wavelength.

3.2.6 Crosstalk

1. Project a small pinhole image on the detector (FWHM ~ 2 μm , compared to the pixel size of 25 μm).
2. Obtain images using an exposure time such that the signal-to-noise ratio of the image is >20 .
3. Repeat step two after moving the pinhole image through a 2x2 pixel grid with $1/10^{\text{th}}$ pixel spacing (2.5 μm).
4. At each point compute $(T-B)/(T+B)$ where T is the number of events reported by the top half per integration time and B is the same from the bottom half. Ideally, this quantity should have an abrupt step from -1 to $+1$ as the spot is scanned across the center line. Because of diffusion, the transition is not abrupt, but graded or sigmoidal. Because of crosstalk the asymptotic values are not -1 and $+1$, but smaller values. Using elementary probability calculations, you can convert that asymptotic value to a nearest-neighbor triggering probability. For example, -0.6 to $+0.6$ corresponds to a triggering probability of 0.115.

3.2.7 Intrapixel Response

1. Project a small pinhole image on the detector (FWHM ~ 2 μm , compared to the pixel size of 25 μm).
2. Obtain an image using an exposure time such that the signal-to-noise ratio of the image is >20 .

3. Repeat step two after moving the pinhole image through a 2x2 pixel grid with $1/10^{\text{th}}$ pixel spacing ($2.5 \mu\text{m}$).
4. Make a contour plot of the measured signal within a 10x10 pixel grid centered on the 2x2 pixel square described in step three as a function of spot location.
5. Make a contour plot of the ratio of measured signal within the central pixel to measured signal within a 10x10 pixel grid centered on the central pixel.

3.3 Milestone Validation Procedure

The measurements in section 3.2 shall be made within a two week time span without warming up the detector. They shall be repeated three times. This sequence shall then be repeated after particle irradiation, during which, the dark count rate experiment shall be executed after a fixed set of doses. The required radiation will be in the form of a high energy proton beam, having ~ 63 MeV energy ($\pm 10\%$), with spatial uniformity of $\pm 10\%$ across the detector, absolute calibrated flux levels of $\pm 10\%$, delivered in geometrically-spaced dose increments from 1 krad (Si) up to 50 krad (Si). A small subset of measurements, including dark current and a measurement of failed pixels, will be performed in between doses.

The results will be verified against success criteria.

4. Success Criteria

The following are the required elements of the milestone demonstration. Each element includes a brief rationale.

4.1. One or more Geiger-Mode Avalanche Photodiode arrays will be fabricated with a high fill-factor, as described in Section 2.3, with a 256x256 format and a pixel size of 25 microns.

Rationale: The high-fill factor and 256x256 array demonstrates the intended format of the GM-APD typical of use for exoplanet missions.

4.2. One GM-APD array described in 4.1 will be tested following the procedure described in Section 3.2 to demonstrate a baseline photon detection sensitivity of 35% at 350 nm, 50% at 650 nm, and 15% at 1000 nm.

Rationale: This provides evidence that the device is functioning nominally at a baseline performance level. Stringent requirements are not placed on the photon detection efficiency, because the goal of this milestone is specifically to demonstrate operation with zero read noise.

4.3. Elements 4.1 and 4.2 must be satisfied for one or more GM-APDs that demonstrate zero read noise, as per the procedure detailed in 3.2.1.

Rationale: A demonstration of zero read noise is the primary goal of this milestone.

4.4. One GM-APD, having previously complied with Elements 4.1–4.3, will be exposed to high energy radiation and tested. The radiation will be in the form of a proton beam, having ~ 63 MeV particles ($\pm 10\%$), with spatial uniformity of $\pm 10\%$ across the detector, absolute calibrated flux levels of $\pm 10\%$, delivered in dose increments no greater than 1 krad (Si), and total doses up to 50 krad (Si). The measurements in Section 3.2 will be performed, and the results will be documented.

Rationale: Radiation testing of the arrays is a crucial step in preparing the devices for flight readiness. Although the results of the tests will be provided, it is the completion of the tests themselves, not a specific performance threshold that marks the completion of this milestone effort. An improved design based on these tests will be the subject of a continuing future effort.

4.5. The pre-radiation tests described in 4.2 and the post-radiation tests described in 4.4 shall be repeated three times without warming up the detector.

Rationale: *The repeated measurements will demonstrate the stability of the performance of the device.*

5. Certification Process

The Principal Investigator will assemble a milestone certification data package for review by the Exoplanet Exploration Program and its Technology Advisory Committee. In the event of a consensus determination that the success criteria have been met, the Program will submit the findings of the TAC, together with the certification data package, to NASA HQ for official certification of milestone compliance. In the event of a disagreement between the Program and the TAC, NASA HQ will determine whether to accept the data package and certify compliance or request additional work.

5.1 Milestone Certification Data Package

The milestone certification data package will contain the following reports and data for each of the 256×256 photon-counting detectors:

- narrative report, including a discussion of how the milestone was met, an explanation of each image or group of images, appropriate tables and summary charts, and a narrative summary of the overall milestone achievement
- description of the low-fill-factor and high-fill-factor GM-APD design and characteristics
- description of the 256×256 CMOS ROIC design and characteristics
- detailed test report of each detector performance property with all significant operating parameters of each experiment
- detailed report of the detector radiation testing with all significant operating parameters
- detailed report of the design changes required to fabricate an improved 256×256 GM-APD with improved dark count rate
- detailed report that identifies additional detector characterization and testing, including design changes in order to have a space quality working device

5.2 The Path to Space Qualification

GM-APD array detectors are at TRL 3, “Analytical and experimental critical function and/or characteristic proof-of concept.” There are several capabilities of these detectors for which “critical function” has been established. These include: 1) single photon event triggering, 2) active avalanche quenching, and 3) triggering and re-arming. The most critical capability of these detectors for the exoplanet application is single photon detection and counting. These functions have been repeatedly validated, as described in a series of papers (Cova et al. 1996, Albota et al. 2002, Marino et al. 2003, Aull et al. 2005, 2006).⁷

This project will validate a photon-counting imager (“component”) in a “laboratory environment” (=TRL 4) and in a simulated mission-like “relevant environment” that includes exposure to high energy radiation, in partial fulfillment of the requirements for TRL 5. Technology advancement activities are shown in Table 3. The green shaded rows of the table

⁷ <http://www.patentstorm.us/patents/7547872.html>

refer to activities in the project. The remaining rows refer to activities that could occur after the project in order to advance the technology to higher TRLs.

Note that as part of the technology advancement, the measured performance will be compared to that predicted by analytical models and competing technologies, e.g. EMCCDs. This process includes the definition of such analytical models at the earlier TRLs. During the current activity, a relevant sensitivity metric will be developed. One likely candidate for such a metric is SNR versus fluence normalized to an ideal detector (c.f. Figures 4 and 10 in Daigle et al. 2008).

Technology Advancement Activities
Activity 1: Validate performance of low-fill-factor 256x256 25 μ m detector. Compare sensitivity to expected performance.
Activity 2: Validate performance of high-fill-factor 256x256 25 μ m detector. Document definition of relevant environment. Compare sensitivity to expected performance.
Activity 3: Validate post-radiation performance of 256x256 25 μ m detectors. Compare sensitivity to expected performance.
Activity 4: Fabricate process lot of GM-APDs
Activity A: Validate performance of high-fill-factor 1024x1024 15 μ m detector. Compare sensitivity to expected performance.
Activity B: Validate post-rad performance of high-fill-factor 1024x1024 15 μ m detector. Compare sensitivity to expected performance.

Table 3. Table of technology advancement activities. Green entries will occur during the two year project, while white gates are for the long-term (unfunded) goals. Note that for this program, the “at risk,” stressed components (as defined in the “Relevant Environment” paragraph of NPR-7120.8 Appendix J), are the effects of radiation exposure. Techniques for packaging, shock testing, thermal-vacuum testing, etc. will be the same legacy procedures as used on previous NASA programs including CHANDRA, ASCA, SUZAKU, and HETE. “Compare sensitivity to expected performance” implies that test performance is documented and compared to predictions from analytical models.

6. References

- Albota MA, Heinrichs RM, Kocher DG, Fouche DG, Player BE, O'Brien ME, Aull BF, Zayhowski JJ, Mooney J, Willard BC, Carlson RR. 2002, "Three-dimensional imaging laser radar with a photon-counting avalanche photodiode array and microchip laser," *Appl Opt.* 2002 Dec 20;41(36):7671-8
- Aull, B. F. "3D Imaging with Geiger-mode Avalanche Photodiodes," *Optics and Photonics News* 16, 42-46 (2005)
- Aull, B., Burns J., Chen C., Felton B., Hanson H., Keast C., Knecht J., Loomis A., Renzi M., Soares A., Suntharalingam V. Warner K., Wolfson D., Yost D., Young D., "Laser radar imager based on three-dimensional integration of Geiger-mode avalanche photodiodes with two SOI timing-circuit layers," *ISSCC Dig. Tech. Papers*, pp 304-305 (2006)
- Cova, S., M. Ghioni, A. Lacaita, and F. Zappa, "Avalanche photodiodes and quenching circuits for single-photon detection," *Applied Optics* 35, 1956-1976, 1996
- Daigle, O., Gach, J.-L., Guillaume, C., Lessard, S., Carignan, C., & Blais-Ouellette, S. 2008, "CCCP: a CCD controller for counting photons," *SPIE*, 7014, pp. 70146L-70146L-10
- Daigle, O., Carignan, C., Gach, J. L., Guillaume, C., Lessard, S., Fortin, C. A., & Blais-Ouellette, S. 2009, "Extreme Faint Flux Imaging with an EMCCD," *PASP*, 121, 866
- Daly, E. et al. 2004, "Standards for Space Radiation Environments and Effects," *ESA Special Publication*, 536, 175
- Figer, D.F., Agronin, M., Balleza, J., Barkhouser, R., Bergeron, L., Greene, G. R., McCandliss, S. R., Rauscher, B. J., Reeves, T., Regan, M. W., Sharma, U., Stockman, H. S. 2003, "The Independent Detector Testing Laboratory and the NGST Detector Program," *SPIE*, 4850, 981
- Figer, D.F., Rauscher, B. J., Regan, M. W., Morse, E., Balleza, J., Bergeron, L., & Stockman, H. S. 2004, "Independent Testing of *JWST* Detector Prototypes," *SPIE*, 5167, 270
- Figer, D.F., Regan, M., Morse, E. & Balleza, J. 2005, "Independent Testing of Silicon PIN Detector Arrays for LSST," *AAS*, 205, 108.08
- Hadwen, B. J.; Camas, M. A.; Robbins, M. S. 2004, "The Effects of Co ⁶⁰ Gamma Radiation on Electron Multiplying Charge-Coupled Devices," *IEEE Transactions on Nuclear Science*, vol. 51, issue 5, pp. 2747-2752
- Marino, R. M., T. Stephens, R. E. Hatch, J. L. McLaughlin, J. G. Mooney, M. E. O'Brien, G. S. Rowe, J. S. Adams, L. Skelly, R. C. Knowlton, S. E. Forman, & W. R. Davis 2003, "A compact 3D imaging laser radar system using Geiger-mode APD arrays: system and measurements," *SPIE Vol. 5086*, 1-15
- Pool, P. J., Morris, D. G., Burt, D. J., Bell, R. T., Holland, A. D., & Smith, D. R. 2005, "Application of electron multiplying CCD technology in space instrumentation," *Proc. of SPIE Vol. 5902*, 67
- Rauscher, B. J., Figer, D. F., et al. 2004, "Detectors for the James Webb Space Telescope near-infrared spectrograph," *SPIE Vol. 5487*, 710
- Simms, L., Figer, D. F. et al. 2007, "First results with a 4Kx4K Si PIN detector," *SPIE*, 6619
- Smith, David R., Ingley, Richard, and Holland, Andrew D. 2006, "Proton Irradiation of EMCCDs," *IEEE Transactions on Electron Devices*, Vol. 53, No. 2
- Trauger, J.T., & Traub, W.A. 2007, "A laboratory demonstration of the capability to image an Earth-like extrasolar planet," *Nature*, 446, 771
- Westhoff, Richard C., Michael K. Rose, James A. Gregory, Gregory D. Berthiaume, John F.

- Seely, Thomas N. Woods, & Gregory Ucker 2007, "Radiation-Hard, Charge-Coupled Devices for the Extreme Ultraviolet Variability Experiment," SPIE Vol. 6686
- Westhoff, Richard C., Reich, Richard C., Loomis, Andrew H., & Gregory, James A. 2007, "Integrated Processes for Detector Back Illumination," Proc, 2007 International Image Sensor Workshop
- Wolf, N.J., Smith, P. S. Traub, W. A. and Jucks, K. W. 2002, "The Spectrum of Earthshine: A Pale Blue Dot Observed from the Ground," ApJ, 574, 430

7. Team Members and Affiliations

<i>Name</i>	<i>Affiliation</i>	<i>Task</i>
Donald F. Figer	RIT	PI - Overall responsibility
Brian Aull	LL	Co-I – APD design and device hybridization
Daniel Schuette	LL	Co-I – ROIC design and testing
Bob Reich	LL	Co-I – Management oversight
Joong Lee	RIT	Radiation testing design and execution
Brandon Hanold	RIT	Detector testing design and integration
Tom Montagiano	RIT	Data acquisition and reduction
Don Stauffer	RIT	Software design
Brian Ashe	RIT	Management

8. Glossary

\bar{c}	counted events
CCD	charge coupled device
CMOS	complementary metal oxide semiconductor
CTE	charge transfer efficiency
e^-	electron
FITS	flexible image transport system
FWHM	full width at half maximum
HFF	high fill factor
L2	Lagrange point #2
LIDAR	LIght Detection And Ranging
LL	Lincoln Laboratory
MOSIS	Metal Oxide Semiconductor Implementation Service
NIEL	nonionizing energy loss
RIDL	Rochester Imaging Detector Laboratory
RIT	Rochester Institute of Technology
ROIC	readout integrated circuit
SNR	signal-to-noise ratio
SPACERAD	abbreviation for Space Environment and Effects Modeling Software product
SPENVIS	Space Environment Information System
SRIM	Stopping and Range of Ions in Matter
TID	total integrated dose
TRL	technology readiness level